Low-temperature solution-processed wavelength-tunable perovskites for lasing

Xing, Guichuan; Mathews, Nripan; Lim, Swee Sien; Yantara, Natalia; Liu, Xinfeng; Sabba, Dharani; Grätzel, Michael; Mhaisalkar, Subodh; Sum, Tze Chien

2014

Xing, G., Mathews, N., Lim, S. S., Yantara, N., Liu, X., Sabba, D., et al. (2014). Low-Temperature Solution-Processed wavelength-Tunable perovskites for lasing. Nature Materials, in press.

https://hdl.handle.net/10356/79520

https://doi.org/10.1038/nmat3911

Low-Temperature Solution-Processed Wavelength Tunable Perovskites for Lasing

Guichuan Xing[1]†, Nripan Mathews[2,3,4]†*, Swee Sien Lim[1,3], Natalia Yantara[2,3], Xinfeng Liu[1], Dharani Sabba [2,3], Michael Grätzel[3,5], Subodh Mhaisalkar[2,3], Tze Chien Sum[1]*

[1]Division of Physics and Applied Physics, School of Physical and Mathematical Sciences, Nanyang Technological University, 21 Nanyang Link, Singapore 637371.

[2]School of Materials Science and Engineering, Nanyang Technological University, Nanyang Avenue, Singapore 639798.

[3]Energy Research Institute @NTU (ERI@N), Research Techno Plaza, X-Frontier Block, Level 5, 50 Nanyang Drive, Singapore 637553.

[4]Singapore-Berkeley Research Initiative for Sustainable Energy, 1 Create Way, Singapore 138602, Singapore.

[5]Laboratory of Photonics and Interfaces, Department of Chemistry and Chemical Engineering, Swiss Federal Institute of Technology, Station 6, CH-1015 Lausanne, Switzerland.

*Correspondence to: Tzechien@ntu.edu.sg; Nripan@ntu.edu.sg

†These authors contributed equally.

Low-temperature solution-processed materials that show optical gain and can be embedded into a wide range of cavity resonators are attractive for the realization of on-chip coherent light sources. Organic semiconductors and colloidal quantum dots (QDs) are considered the main candidates for this application. However, stumbling blocks in organic lasing[1-4] include intrinsic losses from bimolecular annihilation and the conflicting requirements of high charge carrier mobility and large stimulated emission; whereas challenges pertaining to Auger losses and charge transport in QDs[5-7] still remain. Herein, we reveal that solution-processed organic-inorganic halide perovskites ($CH_3NH_3PbX_3$ where X = Cl, Br, I), which demonstrated huge potential in photovoltaics[8-11], have also promising optical gain. Their ultra-stable amplified spontaneous emission (ASE) at strikingly low thresholds stems from their large absorption coefficients, ultralow bulk defect densities, and slow Auger recombination. Straightforward visible spectral tunability (390-790 nm) is demonstrated. Importantly, in view of their balanced ambipolar charge transport characteristics[8] these materials may show electrically driven lasing.

Organic-inorganic halide perovskites have recently emerged as a new class of photovoltaic materials with high efficiencies driven by the large absorption coefficients and long-range balanced electron and hole transport lengths[8-11]. Surprisingly, we found that it also exhibits excellent coherent light emission properties. Figure 1a shows the transition from spontaneous emission (SE) to ASE with increasing pump fluence in a 65 nm thick $CH_3NH_3PbI_3$ film spun-coated on a quartz substrate. At low pump levels, the broad SE (with full width at half maximum (FWHM) ~50 nm, Fig. 1b) from $CH_3NH_3PbI_3$ increases linearly with increasing pump fluence. Correspondingly, the average transient PL lifetimes (τ_{PL}) progressively decreases (Fig. 1b). Above the threshold fluence (12 ± 2 μJ cm^{-2} – see Fig. 1c), the emission intensity increases

superlinearly with τ_{PL} dramatically shortened due to the occurrence of a new short lifetime (< 10 ps) dynamical process (Supplementary Information). Concurrently, the emission band collapses to yield a sharp peak at 788 nm (Fig. 1a). These are clear signatures of optical amplification of the SE from $CH_3NH_3PbI_3$ – *i.e.*, ASE behavior. The balance between optical gain and self-absorption gives rise to the red-shifted ASE peak that is located near the tail of the absorption edge (Supplementary Information)[12]. In this work, we focus on the intrinsic gain properties of perovskites by examining the ASE behavior in a cavity free configuration. The ASEs provide a better benchmark for comparing different material sets on their intrinsic suitability for gain applications. From the measured threshold fluence (12 ± 2 μJ cm^{-2}) and absorption coefficient (α = 5.7×10^4 cm^{-1} at 600 nm – Supplementary Information), ASE threshold carrier density is calculated to be ~1.7×10^{18} cm^{-3}. The threshold carrier density corresponds to the ease at which a material can attain net gain through optical or electrical generated means. Comparatively for highly crystalline high temperature grown ZnSe and CdS nanowires (with similar $\alpha \sim 10^5$ cm^{-1} at the excitation wavelengths), the typical threshold carrier densities are near one order larger under similar measurement conditions[13,14]. Similarly, the typical ASE threshold carrier density for solution processed organic thin films is approximately one order larger[1-4]. As a point of comparison, state-of-the-art cavity-free solution processed polymer films such as poly[9,9-dioctylfluorene-co-9,9-di~4-methoxyphenyl)-fluorene] (F8DP)[15] and Super Yellow[2] exhibited an ASE threshold of ~6 μJ cm^{-2} (calculated from the reported threshold pump energy of 0.1μJ per pulse; excitation stripe 400 μm × 4 mm) and ~36 μJ cm^{-2} (calculated from the reported values of 315 nJ/pulse over a rectangular spot of length 2.5 mm and width ~350 μm) respectively. Our present results on $CH_3NH_3PbI_3$ also compare favorably to a recent breakthrough in CdSe/ZnCdS core/shell colloidal QD films where an ASE threshold of 90 μJ cm^{-2} was reported[5].

Photoluminescence quantum yield (PLQY) approaching 20% at pump fluence above the ASE thresholds were also measured using an integrating sphere (Supplementary Information). The relatively low yield may be a consequence of the low exciton binding energy (19 ± 3 meV)[16] as well as high electron and hole mobilities[17]. Nonetheless, variable stripe length (VSL) measurements on $CH_3NH_3PbI_3$ revealed gain of ~250 cm^{-1} (fitted with Chan's method[7] typically used for colloidal QDs) or ~40 cm^{-1} (fitted with Shaklee and Leheny's method[18] largely used for films of conjugated polymers) at a pump fluence of 14 μJ cm^{-2} (Supplementary Information). These gain values obtained from the respective methods compare favorably with those for colloidal QDs[5,19] and conjugated polymer thin films[20] at comparable excitation intensities.

The noteworthy performances of $CH_3NH_3PbI_3$ with respect to other solution processed systems, present a compelling case to understand the origins driving gain amplification in this system. In particular, we seek to examine why the typical competing non-radiative pathways that can rapidly deplete the carrier population and make ASE unfavorable in other solution processed semiconductors, are not dominant here. These non-radiative pathways include: (i) bulk defects (such as vacancies, interstitials, antisites *etc.*) with fast trapping in the fs to ps timescales[21,22]; (ii) surface/interfacial traps which typically require >100 ps for carrier diffusion through few tens of nanometers of the material[8]; and (iii) multi-particle loss mechanisms (such as bimolecular recombination in organic thin films or Auger recombination in QDs)[1-7].

Following photo-excitation across the $CH_3NH_3PbI_3$ bandgap (at low pump fluence where Auger recombination is not dominant), the excited charge carriers could either relax through bandedge emission or trap-mediated non-radiative pathways. The former gives rise to SE with lifetime (τ_0) and SEM of 4.5 ± 0.3 ns (Fig. 1b). An estimate of the bulk and surface trap densities can be made under these conditions where trap state recombination is much slower than

bandedge radiative recombination. The photo-generated charge carrier density ($n_C(t)$) after photoexcitation can be described with a set of differential equations (see Supplementary Information). The model reveals the presence of two types of traps in these $CH_3NH_3PbI_3$ thin films, with the bulk (surface/interfacial) traps exhibiting fast (slow) trapping times[8,21,22]. The bulk trap density is $n_{TP}^{F} \sim 5\times10^{16}$ cm^{-3} while the surface/interfacial trap density is $n_{TP}^{S} \sim 1.6\times10^{17}$ cm^{-3}. The trap densities measured in $CH_3NH_3PbI_3$ are comparable to defect densities in highly ordered organic crystals (10^{15}-10^{18} cm^{-3})[23] and superior to that of solution processed organic thin films (10^{19} cm^{-3})[24]. Solution deposited, high-temperature annealed Cu-In-Ga-S/Se (CIGS) chalcogenide layers[25] also display comparable defect densities to that reported here (10^{16} cm^{-3}). These low bulk defect densities in perovskite are also consistent with the high solar cell efficiencies in this material[8-11].

To examine the effects of the more prevalent surface/interfacial traps on the carrier dynamics and ASE, PL measurements on bare $CH_3NH_3PbI_3$ were compared against $CH_3NH_3PbI_3$/[6,6]-phenyl-C61-butyric acid methyl ester (PCBM), C_{60}) bilayers to mimic the presence of infinite interfacial electron trap states. Selective excitation of the $CH_3NH_3PbI_3$ layer (~65 nm thick for both cases) was performed with 600 nm laser pulses. The presence of the PCBM layer (~45 nm) is expected to severely quench the SE from the $CH_3NH_3PbI_3$ layer – see Fig. 2a for the PL spectra and Fig. 2b for the PL decay transients. Such efficient PL quenching originates from the long range electron diffusion in the $CH_3NH_3PbI_3$ film, where the diffusion limited electron trapping time by the surface/interface states can be estimated to be ~0.40 ns[8]. Surprisingly, under high pump fluence excitation, the ASE is impervious to the presence of the PCBM layer which acts as a perfect electron quencher. Figure 2b clearly shows that the carrier avalanche proceeds at a much faster timescale than the carrier trapping at the surface/interfacial

states. Thus the surface/interfacial states will not affect the ASE processes, only the fast bulk traps. Indeed, the ASE threshold fluence for the $CH_3NH_3PbI_3$/PCBM film is measured to be 10 ± 2 μJ cm^{-2} (Fig. 2c). This value is slightly smaller than that of the bare $CH_3NH_3PbI_3$ film (12 ± 2 μJ cm^{-2}) because of the better light confinement and propagation due to the presence of the PCBM cladding layer which improves gain buildup (see Supplementary Information). Remarkably, ASE can also be observed in functional photovoltaic devices (η = 11.4%; Device structure: FTO/TiO_2 compact layer/ TiO_2 mesoporous layer/ $CH_3NH_3PbI_3$/ Spiro-OMeTAD/ Au) with optical excitation – see Supplementary Information. The presence of the Spiro-OMeTAD layer which acts as a perfect hole quencher, has no effect on the ASE from $CH_3NH_3PbI_3$ – further exemplifying its exceptional gain properties.

Although low bulk defect density is favourable for obtaining reduced ASE thresholds, a critical criterion for achieving ASE is suppressed multi-particle non-radiative recombination rates (*e.g.*, bimolecular recombination noted in organics or Auger recombination in inorganic semiconductors). Bimolecular recombination (which is a limiting process in organic lasing) have been reported to be extremely low in $CH_3NH_3PbI_3$ – defying the Langevin recombination limit by at least 4 orders of magnitude[17]. These low bi-molecular charge recombination constants are consistent with our findings of low bulk defect densities as discussed earlier. The Auger recombination process in perovskite, which manifest under high pump fluence (nonlinear regime), typically yields Auger lifetimes (τ_{Auger}) from a few ps to ns depending on the photo-generated charge carrier density[6]. The Auger recombination in $CH_3NH_3PbI_3$ is efficient ($\tau_{Auger} \sim 300$ ps) compared to SE (4.5 ± 0.3 ns) because of the long range electron-hole diffusion lengths within them[8]. However, the timescale for the occurrence of ASE (< 10 ps – limited by the instrument response) signifies that the carrier build-up time for population inversion and the

subsequent avalanche, out-competes the Auger processes in these $CH_3NH_3PbI_3$ thin films (Supplementary Information). In contrast to solution processed colloidal QDs (typical biexciton τ_{Auger} ~ 50 ps for 5 nm diameter CdSe QDs)[6], such Auger loss mechanism is less dominant in this "bulk-like" $CH_3NH_3PbI_3$ film.

The photo-stability of the $CH_3NH_3PbI_3$ thin films were assessed by monitoring the ASE intensity as a function of time under laser irradiation at 1 KHz repetition rate at room temperature. Figure 3a shows the variation in ASE intensity with a standard deviation of 0.2 % about the mean intensity for ~26 hours of continuous irradiation (*i.e.*, ~10^8 laser shots in all). The near invariance of the output intensity bears testimony to the excellent optical stability of these perovskite gain media. This performance compares favorably against the state-of-the-art organic semiconducting thin films (50% drop in output power after ~10^7 laser shots)[4] and colloidal QDs (50% drop in output power after ~10^6 laser shots)[7]. The impressive ASE stability of the perovskite layers is also evident from tests of perovskite solar cells irradiated for ~8 hours under ambient conditions (Supplementary Information).

In the absence of any significant defect concentrations, the SE originates from the bandedge emission. Since the SE provides the seed photons for the photon cascade in ASE, the ASE wavelengths are in turn dependent on the bandgap of the semiconducting film. This is clearly evident from our temperature dependent studies where an increase in the bandgap due to a tetragonal to orthorhombic phase transition results in a blue shifted SE and a corresponding shift in the ASE (Fig. 3b)[26]. The orthorhombic phase gives rise to three emission peaks attributed to two bound excitons emissions (815 nm and 782 nm) and a free exciton emission (746 nm), which yields the low temperature ASE peak (at a threshold fluence of 10 ± 2 μJ cm^{-2}). Such intrinsic dependence of the ASE on the bandgap allows for wavelength tunability through halide

substitution. By either using mixtures of bromides and iodides or chlorides and iodides, the band gap is continuously tunable over the entire visible spectral range (from ~390 – 790 nm). We realize this through a simple physical mixing of the precusor solutions prior to spin coating. Figure 3c shows the ASE from $CH_3NH_3PbCl_3$, $CH_3NH_3PbCl_{1.5}Br_{1.5,}$ $CH_3NH_3PbBr_3$, $CH_3NH_3PbBrI_2$ and $CH_3NH_3PbI_3$, thin films, demonstrating its wide wavelength tunability. The ability of the perovskites to encompass the full visible spectrum, allows it to address the "green gap" seen in III-nitrides and III-phosphides[27]. Lasing in perovskites can be achieved with a suitably designed cavity resonator (e.g. with microspheres as whispering galley mode lasing or with gratings as distributed feedback lasing). Towards this, lasing has also been observed from $CH_3NH_3PbI_3$ single crystals from dropcasted thin films (Supplementary Information). This shows that despite the relatively lower PLQY measured, the impressive gain, the large absorption cross-section, low defect densities, low bimolecular recombination and slow Auger recombination in $CH_3NH_3PbI_3$ enables lasing.

Our findings show that these organic-inorganic halide semiconductors are a new class of robust solution-processed gain media with highly desirable characteristics. The low ASE threshold and the long range balanced charge carrier diffusion length stems from the low bulk defect density in $CH_3NH_3PbI_3$ films. The highly crystalline PbX_6 three-dimensional network lends crystalline inorganic character to $CH_3NH_3PbX_3$ while maintaining its solution processability. Broad wavelength tunability is possible with both cation and anion replacement[28]. Their low temperature solution processing is highly compatible with unconventional substrates (Supplementary Information), printing technologies and monolithic integration with silicon-based electronics. Together with the long-range balanced electron and hole diffusion[8], high charge carrier mobilities and low bimolecular charge recombination rates[17] as well as large

wavelength range continuously tunable coherent emission, our findings indicate that the simple solution processed $CH_3NH_3PbX_3$ may hold the key to realizing electrically driven solution processed on-chip coherent light sources.

METHODS

Materials preparation. The $CH_3NH_3PbI_3$ films on quartz substrates were prepared by spincoating 10 vol% solutions in DMF. [6,6]-phenyl-C_{61}-butyric acid methyl ester (PCBM) layers were spincoated from a solvent mixture (10mg/ml) of anhydrous chlorobenzene and anhydrous chloroform (1:1 v/v). The samples were put in vacuum for more than 3 days to get rid of any residual solvent before the optical measurements. Mixed halides were prepared by blending appropriate molar ratios of $CH_3NH_3PbI_3$, $CH_3NH_3PbBr_3$ and $CH_3NH_3PbCl_3$ solutions. The solar cells were fabricated using the sequential deposition procedure as previously reported[9,29] and characterized under simulated air mass 1.5 global (AM1.5G) solar irradiation in the dark.

Optical spectroscopy. For femtosecond optical spectroscopy, the laser sources were (i) Coherent Legend^{TM} regenerative amplifier (150 fs, 1 KHz, 800 nm) seeded by a Coherent Vitesse^{TM} oscillator (100 fs, 80 MHz) and (ii) Coherent Libra^{TM} regenerative amplifier (50 fs, 1 KHz, 800 nm) seeded by a Coherent Vitesse^{TM} oscillator (50 fs, 80 MHz). 800 nm wavelength laser pulses were from the regenerative amplifier's output while 400 nm wavelength laser pulses were obtained with a BBO doubling crystal. 600-nm laser pulses were generated from the Coherent TOPAS-C and Coherent OPerA-Solo optical parametric amplifiers. The laser pulses (circular spot, diameter 1.5 mm) were directed to the films under vacuum in a cryostat. The emission from the samples was collected at a backscattering angle of 150° by a pair of lenses into an optical fiber that is coupled to a spectrometer (Acton, Spectra Pro 2500i) and detected by a charge coupled device (Princeton Instruments, Pixis 400B). Time-resolved PL (TRPL) was collected using an Optronis Optoscope^{TM} streak camera system which has an ultimate temporal resolution of ~10 ps. All optical measurements were performed at room temperature except for

ASE from $CH_3NH_3PbCl_3$ (at 150 K). Room temperature photoluminescence quantum yield (PLQY) of the perovskite thin films were measured using an integrating sphere. The samples were excited with 600 nm pulses generated from the Coherent OPerA-Solo. The emission was corrected for CCD and grating responsivity. Room temperature gain measurements were carried out using standard VSL methods. The excitation stripe was focused by a cylindrical lens (with focal length f = 20 cm) to a stripe and the emission collection configuration was the same as described above. The excitation stripe length was varied through an adjustable slit actuated by a micrometer which was placed at the focal line of the cylindrical lens.

References:

1. Kozlov, V. G., Bulovic, V., Burrows, P. E. & Forrest, S. R. Laser action in organic semiconductor waveguide and double-heterostructure devices. *Nature*, **389,** 362-364 (1997).
2. Namdas, E. B. *et al*. Low thresholds in polymer lasers on conductive substrates by distributed feedback nanoimprinting: progress toward electrically pumped plastic lasers. *Adv. Mater*. **21,** 799-802 (2009).
3. Clark, J. & Lanzani, G. Organic photonics for communications, *Nat. Photonics* **4,** 438-446 (2010).
4. Grivas, C. & Pollnau, M. Organic solid-state integrated amplifiers and lasers, *Laser Photonics Rev*. **6,** 419-462 (2012).
5. Dang, C. *et al*. Red, green and blue lasing enabled by single-exciton gain in colloidal quantum dot films. *Nat. Nanotechnol.* **7,** 335-339 (2012).

6. Klimov, V. I. Spectral and dynamical properties of multiexcitons in semiconductor nanocrystals. *Annu. Rev. Phys. Chem.* **58,** 635 (2007).

7. Chan, Y. *et al*. Blue semiconductor nanocrystal laser. *Appl. Phys. Lett*. **86**, 073102 (2005).

8. Xing, G. *et al*. Long-range balanced electron- and hole-transport lengths in organic-inorganic $CH_3NH_3PbI_3$. *Science* **342,** 344-347 (2013).

9. Burschka, J. *et al*. Sequential deposition as a route to high-performance perovskite-sensitized solar cells. *Nature* **499,** 316-319 (2013).

10. Kim, H. S. *et al*. Lead iodide perovskite sensitized all-solid-state submicron thin film mesoscopic solar cell with efficiency exceeding 9%. *Sci. Rep.* **2,** 591 (2012).

11. Heo, J. H. *et al*. Efficient inorganic-organic hybrid heterojunction solar cells containing perovskite compound and polymeric hole conductors. *Nat. Photonics* **7,** 486-491 (2013).

12. Ding, J., Hagerott, M., Ishihara, T., Jeon, H. & Nurmikko, A. V. (Zn,Cd)Se/ZnSe quantum-well lasers: Excitonic gain in an inhomogeneously broadened quasi-two-dimensional system. *Phys. Rev. B* **47,** 10528-10542 (1993).

13. Xing, G. *et al*. Ultrafast exciton dynamics and two-photon pumped lasing from ZnSe nanowires. *Adv. Opt. Mater*. **1,** 319-326 (2013).

14. Liu, X., Zhang, Q., Xiong, Q. & Sum, T. C. Tailoring the lasing modes in semiconductor nanowire cavities using intrinsic self-absorption, *Nano Lett*. **13,** 1080-1085 (2013).

15. Xia, R., Heliotis, G., & Bradley, D. D. Fluorene-based polymer gain media for solid-state laser emission across the full visible spectrum. *Appl. Phys. Lett.* **82**, 3599-3601 (2003).

16. Sun, S. *et al.* The origin of high efficiency in low-temperature solution-processable bilayer organometal halide hybrid solar cells. *Energy Environ. Sci.* **7,** 399-407 (2014).

17. Wehrenfennig, C., Eperon, G. E., Johnston, M. B., Snaith, H. J., Herz, L. M. High Charge Carrier Mobilities and Lifetimes in Organolead Trihalide Perovskites. *Adv. Mater.* DOI: 10.1002/adma.201305172 (2013).

18. Shaklee, K. L., Leheny, R. F. Direct determination of optical gain in semiconductor crystals. *Appl. Phys. Lett*. **18**, 475-477 (1971).

19. Liao, Y., Xing, G., Mishra, N., Sum, T. C. & Chan, Y. Low Threshold, Amplified Spontaneous Emission from Core-Seeded Semiconductor Nanotetrapods Incorporated into a Sol–Gel Matrix. *Adv. Mater.* **24,** 159-164 (2012).

20. Lampert, Z. E., Reynolds Jr, C. L., Papanikolas, J. M., & Aboelfotoh, M. O. Controlling Morphology and Chain Aggregation in Semiconducting Conjugated Polymers: The Role of Solvent on Optical Gain in MEH-PPV. *J. Phys. Chem. B.* **116,** 12835-12841 (2012).

21. Xing, G. *et al*. Charge transfer dynamics in Cu-doped ZnO nanowires. *Appl. Phys. Lett*. **98,** 102105/1-102105/3 (2011).

22. Uhd Jepsen, P. *et al*. Ultrafast carrier trapping in microcrystalline silicon observed in optical pump-terahertz probe measurements. *Appl. Phys. Lett*. **79,** 1291-1293 (2001).

23. Mehraeen, S., Coropceanu, V. & Bredas, J. L. Role of band states and trap states in the electrical properties of organic semiconductors: Hopping versus mobility edge model. *Phys. Rev. B* **87,** 195209/1-195209/9 (2013).

24. Willa, K. *et al*. From organic single crystals to solution processed thin-films: charge transport and trapping with varying degree of order. *J. App. Phys*. **113,** 133707 (2013).

25. Graetzel, M., Janssen, R. A. J., Mitzi, D. B. & Sargent, E. H. Materials interface engineering for solution-processed photovoltaics. *Nature* **488,** 304-312 (2012).

26. Baikie, T. *et al*. Synthesis and crystal chemistry of the hybrid perovskite $(CH_3NH_3)PbI_3$ for solid-state sensitised solar cell applications. *J. Mater. Chem. A* **1,** 5628-5641 (2013).

27. Laubsch, A., Sabathil, M., Baur, J., Peter, M. & Hahn, B. High-power and high-efficiency InGaN-based light emitters. *IEEE T. Electron. Dev.* **57,** 79-87 (2010).

28. Zhang, S. *et al.* Preparations and Characterizations of Luminescent Two Dimensional Organic-inorganic Perovskite Semiconductors. *Materials* **3,** 3385-3406 (2010).

29. Mulmudi, H. K. *et al*. Flexible, low-temperature, solution processed ZnO-based perovskite solid state solar cells. *Chem. Comm.* DOI: 10.1039/C3CC46534A (2013).

Acknowledgements

We would like to acknowledge D. Giovanni for the data fitting and C.W. Kiang for the electroluminescence measurement, as well as S. Shuangyong, J. Chua, T. Krishnamoorthy and S. Kulkarni for sample and precursor preparation. Financial support from NTU start-up grants M4080514 and M4081293, SPMS collaborative Research Award M4080536, Ministry of Education AcRF Tier 2 grant MOE2013-T2-1-081 and from the Singapore NRF through the Competitive Research Program (NRF-CRP4-2008-03) and the Singapore-Berkeley Research Initiative for Sustainable Energy (SinBeRISE) CREATE Programme is gratefully acknowledged. M. G. thanks the European Research Council for financial support under the Advanced Research Grant (ARG 247404) 'Mesolight'.

Author contributions

G. X., N. M. and T. C. S. conceived the idea for the manuscript and designed the experiments. G. X. developed the basic concepts, conducted the spectroscopic characterization and coordinated

the experiments. N. M. and S. D. fabricated and characterized the samples. N. Y., X. L., M. G. and S. M. contributed to the data analysis. T. C. S., N. M., G. X., S. M. and S. S. L. analyzed the data and wrote the paper. T. C. S. and N. M. led the project.

Additional Information

Supplementary information is available in the online version of the paper. Reprints and permissions information is available at www.nature.com/reprints. Correspondence and requests for materials should be addressed to T. C. S. or N. M.

Competing financial interests

The authors declare no competing financial interests.

Figures:

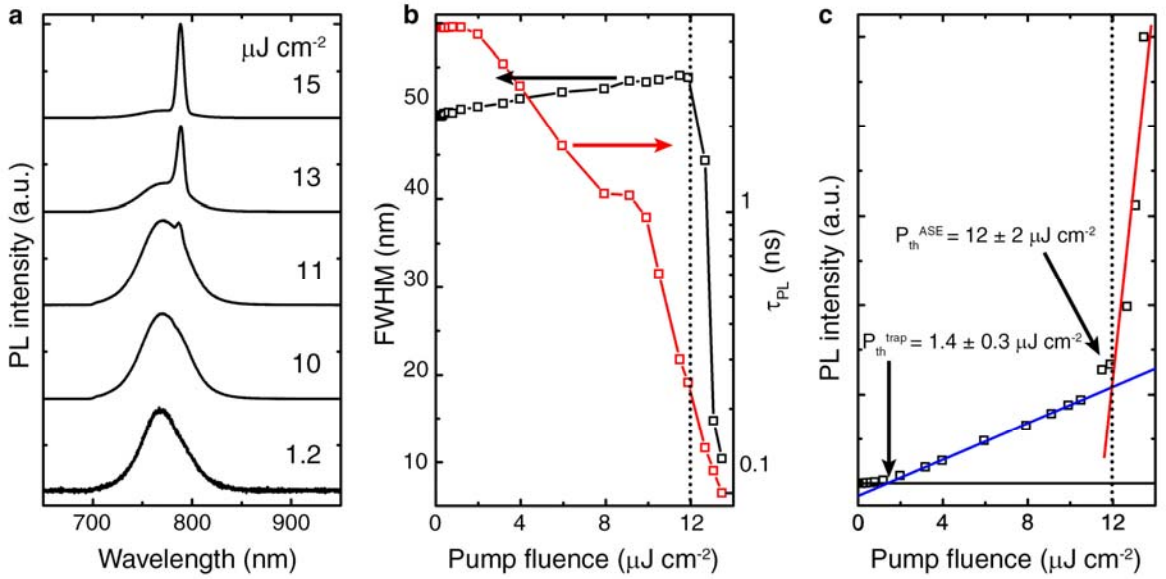

Figure 1 | Coherent light emission from solution processed perovskite film. **a**, Steady-state PL emission spectra from a 65 nm thick $CH_3NH_3PbI_3$ film photoexcited using 600 nm, 150 fs and 1 KHz pump pulses with increasing pump fluence (per pulse) – illustrating the transition from SE to ASE. **b**, FWHM of the emission peak and average transient PL lifetime (τ_{PL}) as a function of the pump fluence. τ_{PL} is the time taken for the intensity to decrease to 1/e of its initial value. **c,** PL intensity as a function of pump fluence. The arrows indicate the trap state saturation threshold and the ASE threshold. The blue and red lines represent the linear fits to experimental data in the two linear regimes of SE and ASE, respectively.

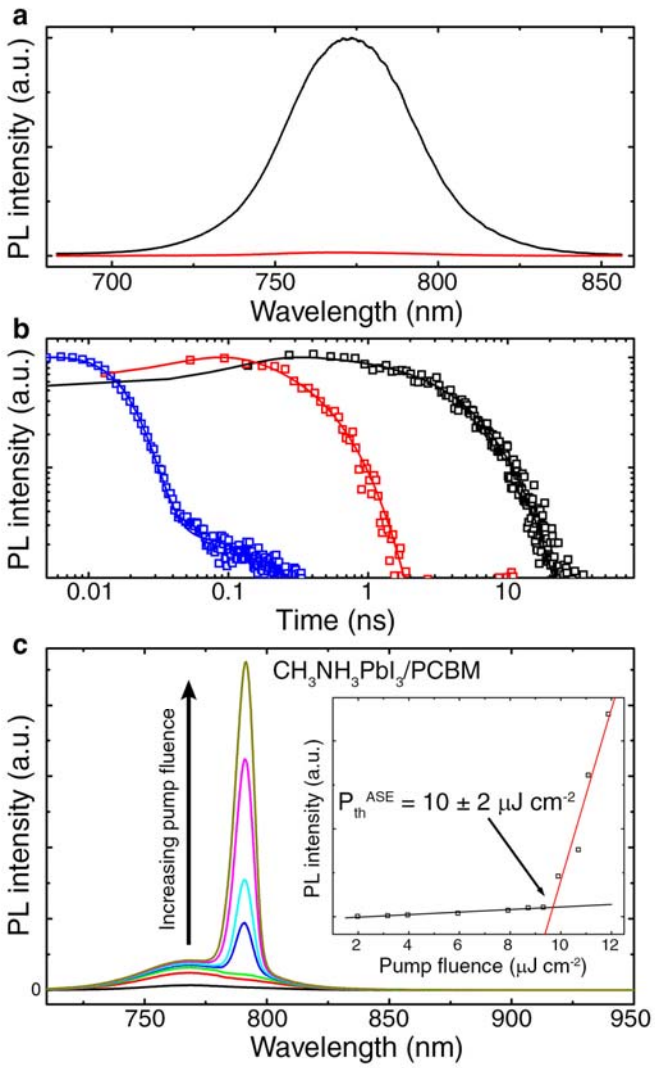

Figure 2 | Effects of surface/interfacial traps on the coherent light emission. a, Time-integrated PL spectra of $CH_3NH_3PbI_3$ (black) and $CH_3NH_3PbI_3$/PCBM (red). **b**, Time-resolved PL (TRPL) decay transients for quartz/$CH_3NH_3PbI_3$(65 nm) (black~1.3 μJ cm^{-2}) and quartz/$CH_3NH_3PbI_3$(65 nm)/PCBM (red~1.3 μJ cm^{-2}, blue~17 μJ cm^{-2}) films in vacuum following excitation at 600 nm (1 KHz, 150 fs). Through modifying the surface/interfacial trap density, these measurements reveal that while SE is strongly quenched by the surface/interfacial traps, ASE which occurs on a much faster timescale could effectively compete with these carrier trapping processes. The solid lines in **b** are the single-exponential fits of the PL decay transients. **c**, The pump fluence dependent PL spectra and PL intensity (inset) of quartz/$CH_3NH_3PbI_3$(65 nm)/PCBM film.

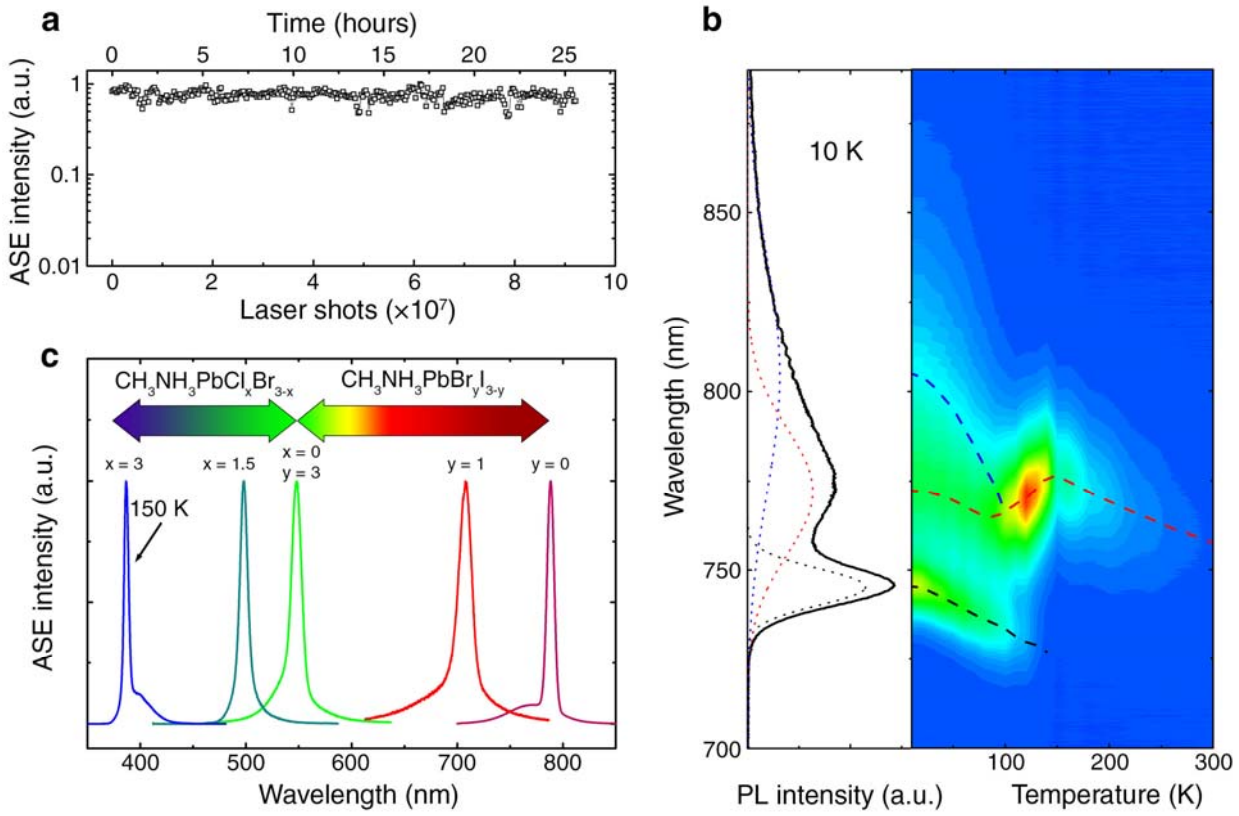

Figure 3 | ASE photo-stability, temperature dependent PL and facile wide emission wavelength tunability. a, Shot-dependent ASE intensity of the solution processed $CH_3NH_3PbI_3$ film with over 9×10^7 laser excitation shots at 600 nm (1 KHz, 50 fs, ~18 μJ cm^{-2}) performed at room temperature. **b**, PL spectrum at 10 K – where the dotted lines are the deconvolved Gaussian peaks. The dashed lines in the false color temperature-dependent PL map show the evolution of the emission peaks with temperature. **c**, Wide wavelength tunability of ASE wavelengths from low-temperature solution-processed organic-inorganic halide perovskite films fabricated by mixing the precursor solutions.